Influence of Cations on Direct CO_2 Capture and Mineral Film Formation: the Role of KCl and $MgCl_2$ at Air/Electrolyte/Iron Interface

Chathura de Alwis, Kayleigh Wahr, Kathryn A. Perrine*
Department of Chemistry, Michigan Technological University, Houghton, MI 49931

*Corresponding author

Supporting Information

Table of Contents **Page Number**

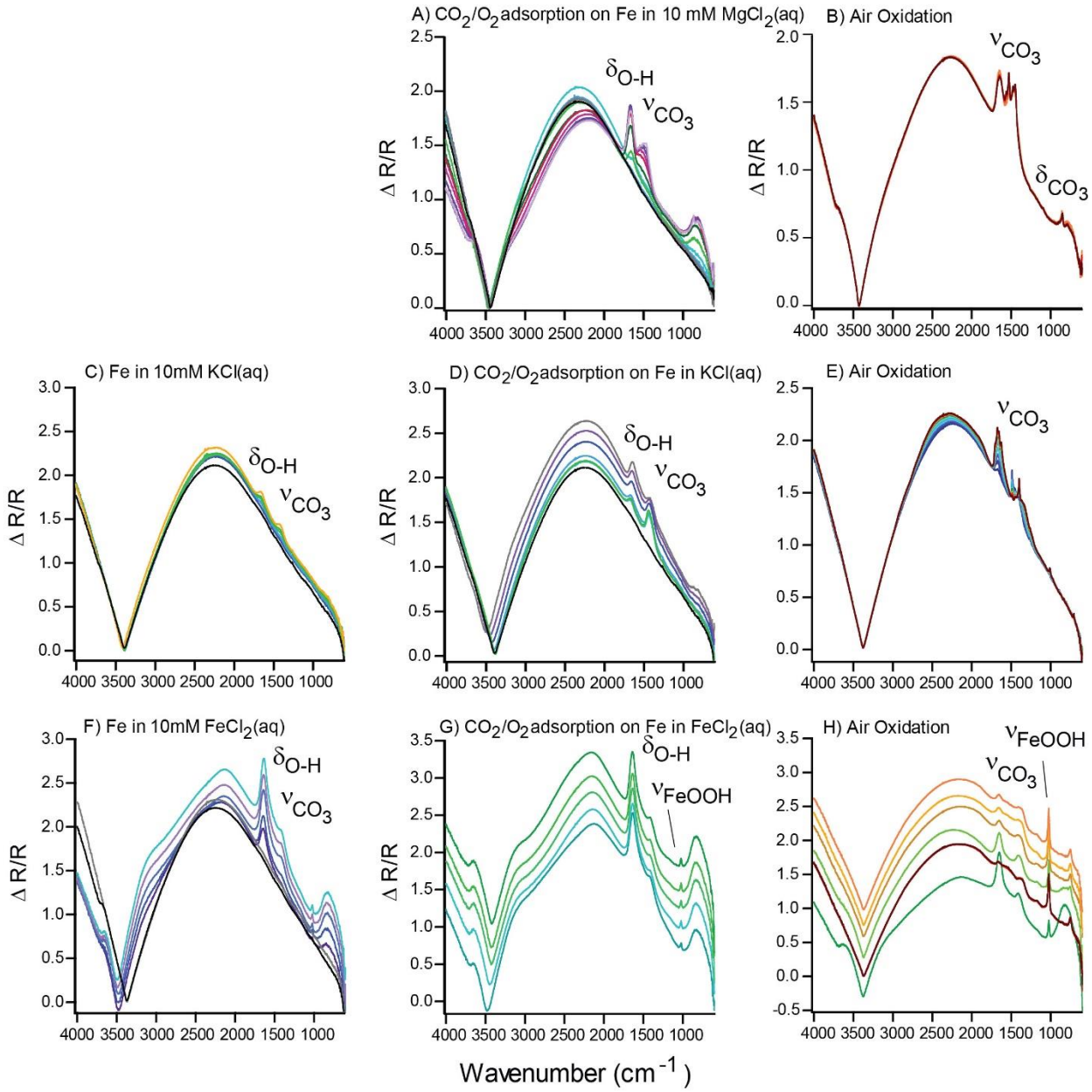

Figure S1: Example raw PM-IRRAS spectra of iron surfaces exposed to 10 mM $MgCl_2$, KCl and $FeCl_2$ electrolytes during each stage with the δOH bending mode and carbonate stretching modes (νCO_3) labeled on the Bessel-shaped background. Reflectance spectra for stage 1 is shown for when Fe is exposed to each electrolyte (graphs C in KCl(aq) and F in $FeCl_2$(aq)). Spectra for stage 2 is shown for the iron interface during oxidation from adsorption of atmospheric CO_2 and O_2: graphs A (in $MgCl_2$(aq)), D (in KCl(aq)), and G ($FeCl_2$(aq)). Spectra for stage 3 of oxidation of the iron surface in air: graphs B (in $MgCl_2$(aq)), E (in KCl(aq)), and H ($FeCl_2$(aq)). Note that no reflectance peaks were observed in stage 1 for Fe in $MgCl_2$(aq) (not shown).

Table S1: Trace metals and their composition (% or ppm) in iron materials for high purity iron (Alfa Aesar) and low purity iron (Allied Metal Corps). Trace anti-corrosion metals may lead to different kinetics in the lower purity iron samples.

manufacturer	**Allied Metal Corps.**	**Alfa Aesar**	
purity	**low purity-99.99%**	**HP-99.995%**	
Element	**% Composition, EFP**	**ppm**	**actual %**
C	0.002	20	0.002
S	0.005	13	0.0013
P	0.004	11	0.0011
Mn	0.070	5.8	0.00058
Si	0.001	30	0.003
Co	0.002	6.4	0.00064
Cu	0.008	1.1	0.00011
Ni	0.016	2	0.0002
Cr	0.0128	15	0.0015
Pb	0.0005	0.02	0.000002
V	0.001	0.29	0.000029
W	0.001	0.09	0.000009
Sn	0.001	0.18	0.000018
Al	0.008	1.2	0.00012
Ti	0.001	0.16	0.000016
B	0.0005	0.09	0.000009
Nb	0.001	0.08	0.000008
N	0.002	10	0.001
As	0.001	0.26	0.000026
Sb	0.001	0.05	0.000005
Mo	0.001	0.6	0.00006

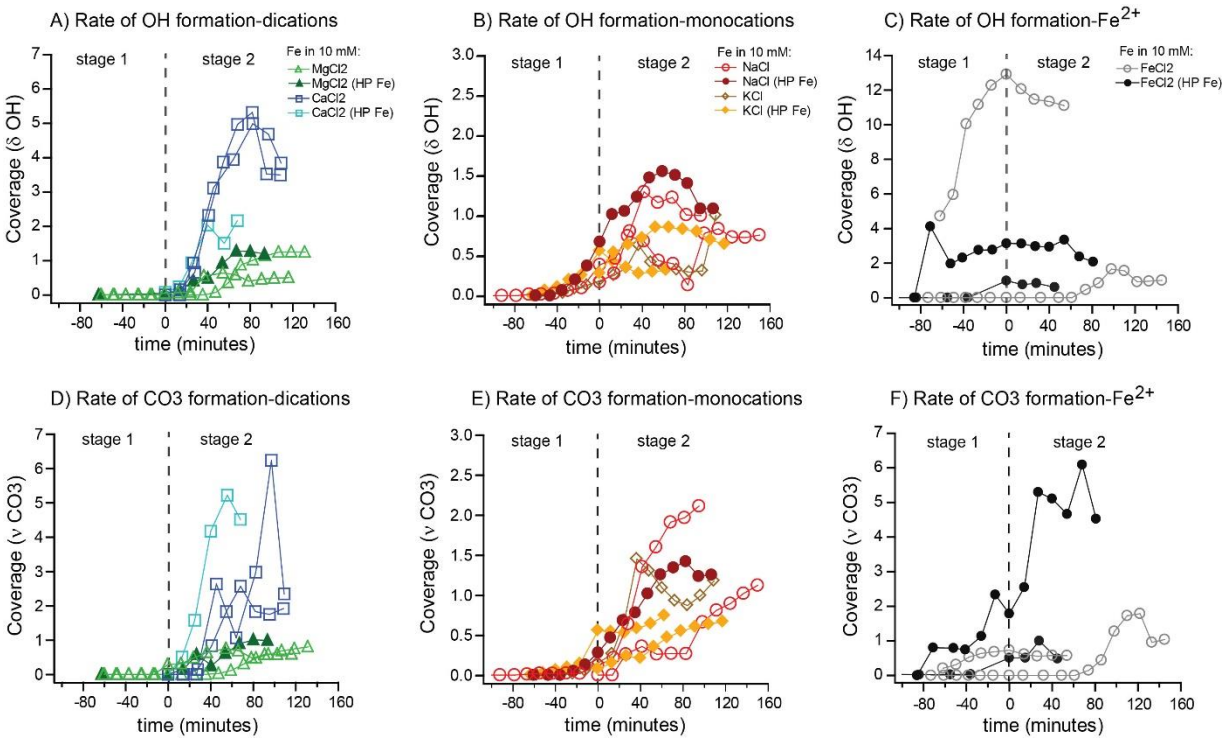

Figure S2: Rates of hydroxylation (top row A-C) and carbonation (D-F) for all electrolytes studied: $MgCl_2$, $CaCl_2$, NaCl, KCl, $FeCl_2$. Similar trends are observed for A and D) $MgCl_2$ (green triangles) and $CaCl_2$ (blue squares) that have high carbonation rates. The Fe samples exposed to B and E) KCl (yellow diamonds) and NaCl (red circles) have similar trends. Fe in D and F) $FeCl_2$ (black and grey circles) initially show initial high carbonation and hydroxylation and then strong oxidation in stage 3. Closed markers are data collected on high purity (99.995%) Fe and open markers are data collected on low purity (99.99%) Fe. Data for Ca and Na chloride solutions in A-B, D-E are reprinted (adapted) with permission from de Alwis, C.; Trought, M.; Lundeen, J.; Perrine, K. A. Effect of Cations on the Oxidation and Atmospheric Corrosion of Iron Interfaces to Minerals. *Journal of Physical Chemistry A* **2021**, *125* (36), 8047-8063. Copyright 2021 American Chemical Society.

Table S2: Rates of hydroxylation and carbonation (s^{-1}) of iron surfaces exposed to each solution for low purity iron samples. For low purity (99.99%) Fe, the trend shows the average rate of hydroxylation is in the order of $K^+ > Na^+ > Fe^{2+}$. The average rate of carbonation increases in the order of $K^+ > Mg^{2+} > Ca^{2+} = Fe^{2+} > Na^+$, which may be attributed to different anti-corrosion metals in the low purity Fe.

Low purity (99.99%) Fe	**stage 1**		**stage 2**	
solution	**δOH**	**νCO₃**	**δOH**	**νCO₃**
$MgCl_2$	n/a	n/a	1.07×10^{-3}	8.24×10^{-4}
$CaCl_2$	n/a	n/a	7.79×10^{-4}	6.77×10^{-4}
KCl	1.01×10^{-3}	1.08×10^{-3}	6.56×10^{-4}	1.48×10^{-3}
NaCl	6.28×10^{-4}	1.64×10^{-4}	2.97×10^{-4}	4.78×10^{-4}
$FeCl_2$	3.56×10^{-4}	-6.68×10^{-5}	2.79×10^{-4}	6.57×10^{-4}

Natural mineral specimen locale: All specimens are loaned courtesy of A. E. Seaman Mineral Museum at Michigan Technological University, unless otherwise noted. Specimen locale information is listed below.

Mg-based minerals:

Magnesite ($MgCO_3$, DM22799), Baymag magnesite mine, Radium Hot Springs, BC, Canada

Hydromagnesite ($Mg_5(CO_3)_4(OH)_2 \cdot 4H_2O$, DM10362), Lodi, Nevada

Nesquehonite ($Mg(HCO_3)OH \cdot 2H_2O$, DM10570) from Nesquehoning, near Schuykill Co., PA

Nesquehonite (#1623) from Nesquehoning, Carbon County, PA; from the Carnegie Museum of Natural History collection

Artinite ($Mg_2(CO_3)(OH)_2 \cdot 3H_2O$, PJC8091), San Benito, California (probably Picacho Peak, New Idria mining district)

Artinite (Cedar Hill Quarry, PA), catalog CM20830 from the Carnegie Museum of Natural History collection

Pokrovskite ($Mg_2(CO_3)(OH)_2 \cdot 0.5H_2O$, MGMH#142816) from Hunting Hill Quarry, Montgomery Co., Maryland, USA; courtesy of the Mineralogical & Geological Museum at Harvard University

Brugnatellite ($Mg_6Fe^{3+}(CO_3)(OH)_{13} \cdot 4H_2O$, DM10381), Mount Ramazzo mine, Borzoli, Near Genova, Liguria, Italy

Coalingite ($Mg_{10}Fe^{3+}_2(OH)_{24}(CO_3) \cdot 2H_2O$, DM25017), Huntington Hill Quarry, Rockville, MD

Other mineral locale information from the main manuscript:

Erythrosiderite ($K_2[FeCl_5(H_2O)]$, DM4156), 1926 eruption of Mt. Vesuvius (Naples, Campania, Italy)

Goethite (α-FeOOH, DM6809), Restormel Mine, Lostwithiel, Cornwall, England

Lepidocrocite (γ-FeOOH, DM-22910), Iron Monarch mine, Iron Knob, Australia

Attenuated total reflectance – Fourier transform infrared (ATR-FTIR) spectroscopy of iron surfaces exposed 10 mM $MgCl_2$(aq) compared to ATR-FTIR spectra of natural minerals and powdered samples. Figure S3 gives an ATR-FTIR spectral comparison of air/$MgCl_2$(aq)/Fe interfacial material and spectra of several Mg bearing natural minerals. There is no exact match for the spectrum of at the air/$MgCl_2$(aq)/Fe interface. However, hydromagnesite, Pokrovsite, and nesquehonite give a partial match of spectral features based on the νOH modes near 3500 cm^{-1}, the νCO_3 signature between 1650-1300 cm^{-1}, and the δCO_3 mode at 855 cm^{-1}. The splitting of the νCO_3 modes between the asymmetric and symmetric modes of the remaining spectra in the right panel do not match the Mg carbonate film grown on the iron surface. Therefore, the interfacial CO_3 layer formed at air/$MgCl_2$(aq)/Fe interface are likely a mixture of magnesium carbonate, hydromagnesite, and a magnesium iron carbonate hydroxide film.

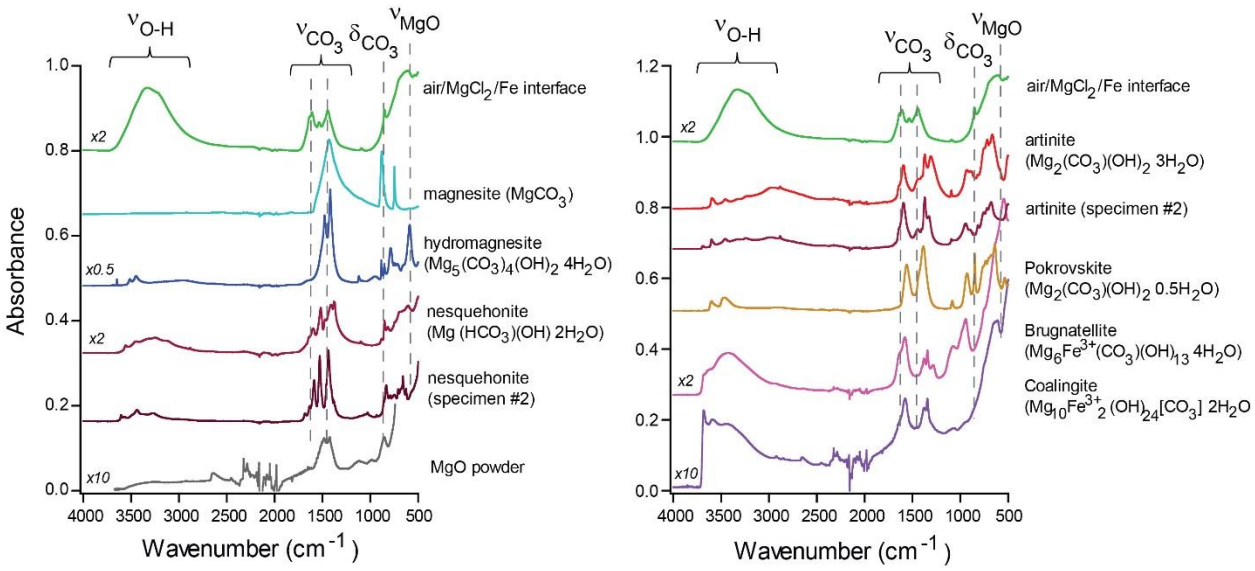

Figure S3: ATR-FTIR spectra of additional natural mineral specimens as compared with the interface region of iron exposed to $MgCl_2$(aq). Dotted lines are shown to guide the eye, aligning with carbonate stretching and deformation modes as well as the Mg-O modes.

Table S3: Assignments of observed modes in the ATR-FTIR spectra of the interface and submerged regions compared to spectral signatures of natural mineral specimens. References for γ-FeOOH and Mg carbonates see refs [1-4]. For bicarbonates modes see refs [5-7].

Sample/ region	**νOH**	**νCO_3 asym (bidendate)**		**νCO_3 asym**	**νCO_3 sym**	**νCO_3**	**νCO_3 sym (mono)**	**MgOH**	**Mg-CO_3**	**δCO_3**	**MgO**	**MgO**	**Mg-O**	**Mg-OH**
Interface $MgCl_2$(aq)/Fe	3335	1632	1609	1535, 1478, 1445			1093			855, 848		702	598, 534	505, 434
Submerged $MgCl_2$(aq)/Fe	3082	1627		1477	1354	1155, 1018					742			430
Magnesite $MgCO_3$				1430					879	855	747			
Hydromagnesite $Mg_5(CO_3)_4(OH)_2$ $4H_2O$	3649, 3513, 3448			1478, 1418		1120	1109	952	884	852, 787	744, 729	713	655, 588	430
Nesquehonite $MgCO_3$ $3H_2O$	3557, 3247	1643	1598	1517, 1472, 1409	1376		1099		880	852, 818	748		696, 605	
Artinite $Mg_2CO_3(OH)2$ $3H_2O$	3596, 2963	1639	1594	1438, 1398	1370, 1309		1093	932	890	817	749, 719	695	667	502
Pokrovsite Mg_2 $CO_3(OH)_2$	3602, 3465		1560	1490	1386		1084	932		848	758, 736	700	639, 536	434
Brugnatellite $Mg_6Fe^{3+}(CO_3)(OH)_{13}$·$4H_2O$	3403	1635	1579	1403	1380, 1344, 1283	1042	1086	957			750		639, 544	423
Coalingite $Mg_{10}Fe^{3+}{}_2(OH)_{24}(CO_3)$·$2H_2O$	3682, 3426	1636	1576		1379, 1345		1068	944			753		629	
MgO powder MgO	3700			1482, 1425		1120		986		856				
	νOH	**νCO_3 /δOH**	**νCO_3**	**νCO_3 asym**	**νCO_3**	**γ-FeOOH**	**νCO_3 sym (mono)**		**δCO_3**	**δCO_3**	**νFe-O**	**δCO /νOH**	**K-O**	**νFe-O**
Interface KCl(aq)/Fe		1637		1481, 1394	1270, 1251	1012				835		695	668, 646	
Submerged KCl(aq)/Fe		1629		1484	1341	1159, 1019					744			530
Erythrosiderite $K_2[FeCl_5(H_2O)$	3354, 3138	1639	1587	1405			1062	939		836, 806			576	533, 441
K_2CO_3 powder	3168				1360		1060		878			706, 691	674, 685	
Bicarbonate $KHCO_3$(aq)/Fe	2931	1615			1362	1005				829		701		
	νOH	**νCO_3 /δOH**		**νCO_3 asym**	**νCO_3**	**γ-FeOOH**			**δ-FeOOH**		**νFe-O**			**νFe-O**
interface $FeCl_2$(aq)/Fe	3057	1627		1478	1351	1153, 1015					743			537, 450
Submerged $FeCl_2$(aq)/Fe	3042	1616		1481	1355	1155, 1020					743			533, 440
Lepidocrocite γ-FeOOH						1139, 1018			893		746			444
Goethite δ-FeOOH	3075	1653		1441		1113			889		789			

ATR-FTIR spectra is shown in Figure S4 of the different regions on the iron samples of the iron surface after exposure to the electrolytes during the PM-IRRAS experiments. For Fe in $MgCl_2$(aq), the interface region is identified as a mixture of magnesite, hydromagnesite, and hydroxycarbonates. For Fe in KCl(aq) a bicarbonate film is grown at the air/solution/Fe interface. In the submerged region, where there is no gradual exposure to atmospheric CO_2 and O_2, there are different regions of interest that were assessed. The region of the sample that is corroded (rusted) is identified as a heterogeneous mixture of γ-FeOOH and Fe oxyhydroxide carbonates ($Fe_x(OH)_2CO_3$).

The submerged regions without corrosion (uncorroded) have carbonate signatures similar to the interface region, but less intense in absorbance, where a thin (non-visible) non-specific carbonate film is present. For the non-corroded Fe region submerged in KCl(aq), the growth of a bicarbonate film is observed, similar to the interface region. Other areas between 1300 cm^{-1} and 1500 cm^{-1} of the uncorroded regions show broad peaks that align with the two doublet carbonate peaks in $MgCl_2$(aq) and a blue corrosion spot for Fe in KCl(aq), which are labeled as non-specific carbonates. The non-specific carbonates may be precursors to the films grown at the interface.

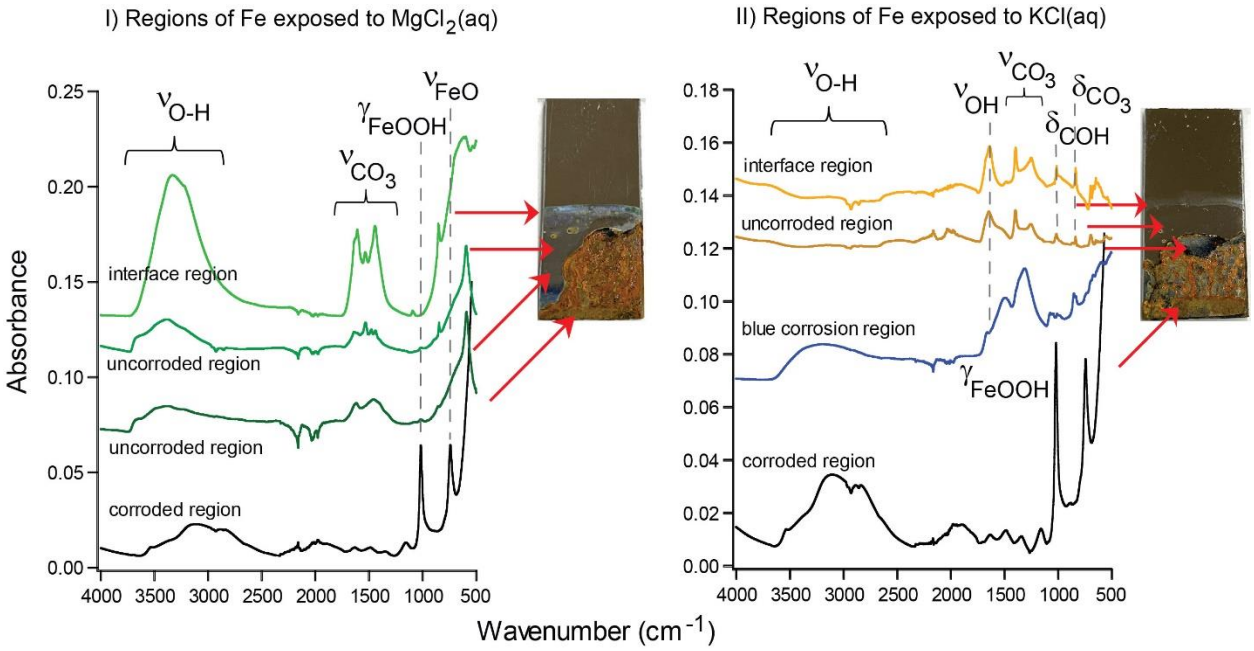

Figure S4: ATR-FTIR spectra of various films grown on different regions on the iron surface after PM-IRRAS experiments for I) Fe exposed to $MgCl_2$(aq) and II) Fe exposed to KCl(aq). Arrows point to region of the sample that were measured. All spectra used the unexposed, polished Fe as the background spectrum.

To check that dissolved carbonates were not contributing to the carbonate film growth, the used solutions after the PM-IRRAS experiments were assessed with ATR-FTIR spectroscopy. Figure S5 compares the ATR-FTIR spectrum of a 0.10 M $KHCO_3$ solution with three solutions used in the PM-IRRAS experiments: 10 mM $FeCl_2$(aq), 10 mM KCl(aq), and 10 mM $MgCl_2$(aq). Water was used as the background. These spectra show bicarbonates or carbonates are not present in the solutions after several (2-4) hours of air exposure. Bicarbonates (HCO_3) concentrations are small and may not be detected in the used solutions, suggesting that the carbonates observed at the interface are grown primarily from exposure of the air/solution/Fe interface to atmospheric CO_2.

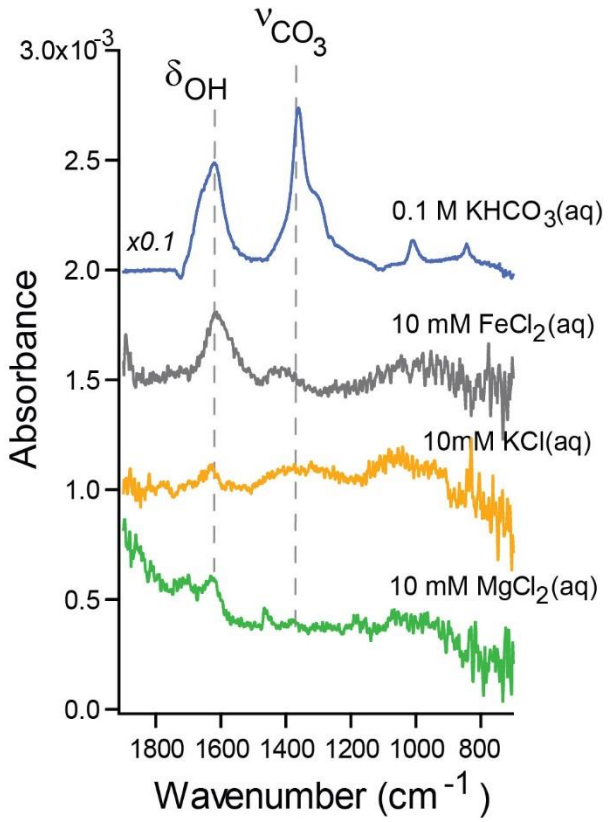

Figure S5: ATR-FTIR spectra of liquid solutions after PM-IRRAS experiments: 10mM $FeCl_2$(aq), KCl(aq), and $MgCl_2$(aq). These are compared to a 0.10 M solution of $KHCO_3$(aq).

Figure S6 shows XPS spectra of the Mg 1s, Fe 3p, and Mg 2p regions of different sample regions after the AFM and PM-IRRAS experiments. Spectrum A) shows the interface region used during AFM experiments (after the sample was rinsed off), spectrum B) the white film, and the C) interface region after PM-IRRAS experiments, all compared to the submerged region in spectrum D. The regions exposed to the $MgCl_2$ solution have two Mg carbonate species. The primary species in the Mg 1s region is at 1304.3 eV, assigned to $MgCO_3$, and the minor species at 1306.9 eV is assigned to MgO.[8, 9] The same species is observed between 49.5-49.8 eV in the Mg 2p region.[10, 11] The polished region of the PM-IRRAS sample, spectrum E, does not contain any Mg species, as expected. The Fe 3p region of the polished iron surface has a binding energy of 55.0 eV from the native oxide layer. After the film is grown on the surface, the binding energy shifts to 55.6 eV. XPS of spectra A) the AFM sample at the droplet interface was collected after rinsing the sample with nanopure water, showing that the remaining $MgCO_3$ is bound to the surface.

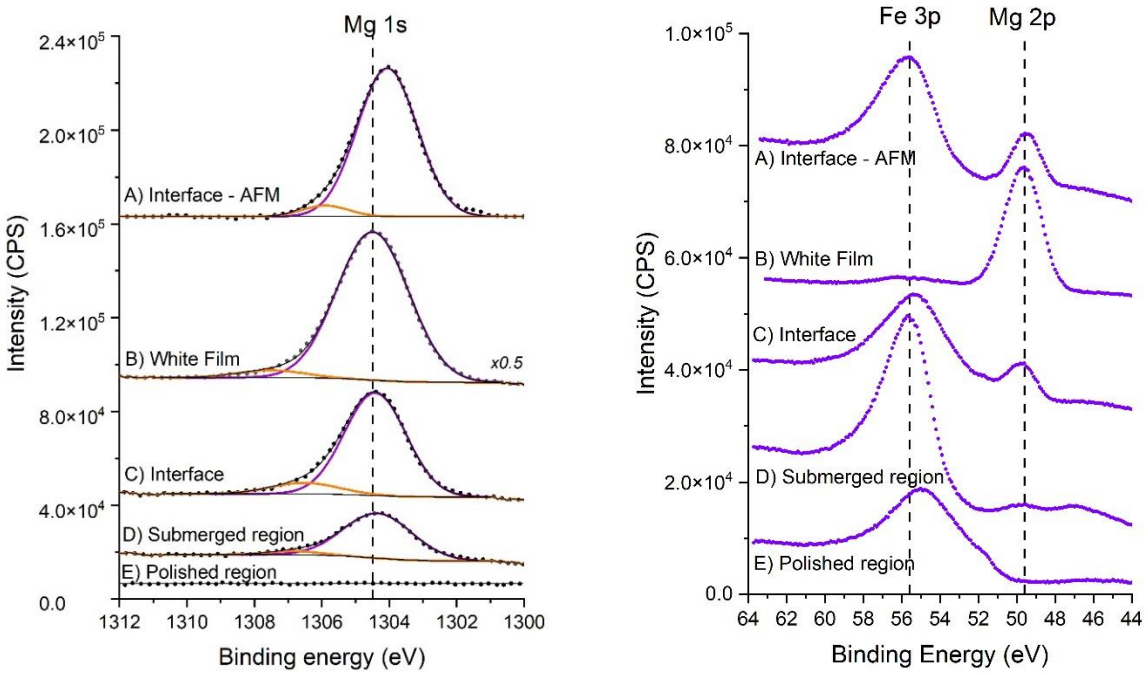

Figure S6: XPS spectra of the Mg 1s, Fe 3p, and Mg 2p regions collected of Fe in $MgCl_2$(aq) solution for (A) the AFM interface region, (B) the white film at the interface of the PM-IRRAS sample, (C) the interface of the PM-IRRAS sample, (D) the submerged region of the PM-IRRAS sample, and (E) the polished (uncorroded) region of the iron surface.

Figure S7 shows a comparison of the XPS Fe 2p regions collected for I) Fe in $MgCl_2$(aq) and II) Fe in KCl(aq). The Shirley background was subtracted from all the spectra. All Fe 2p regions show the Fe surface is oxidized after the experiments, with Fe $2p_{3/2}$ binding energies ranging between 710.6-711.5 eV. The polished region contains a native oxide layer in air. All the other Fe regions shown in the Figure S7I and 7II has undergone oxidation, which produces the Fe^{2+} or Fe^{3+} oxidation state.[12-14] The fact that there are small satellite features in spectra A) the interface region of the AFM samples and C) the submerged regions is that the surface has oxidized and corroded, producing a γ-FeOOH species. These are in contrast to the thick carbonate films grown in the interface region in spectra B, showing reduced satellite intensities.

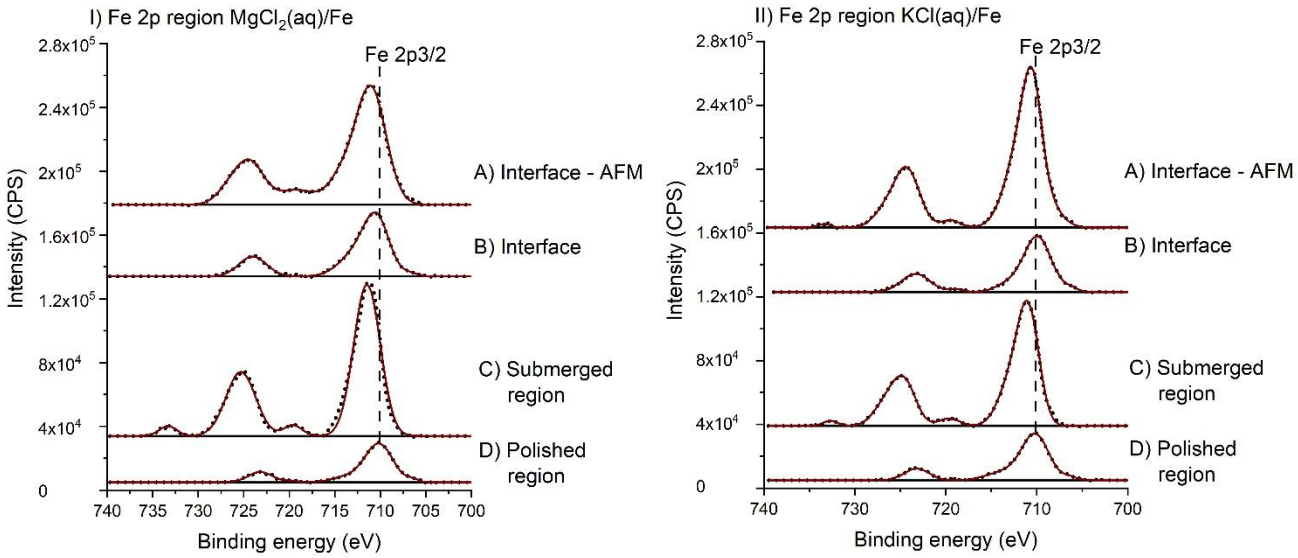

Figure S7: XPS spectra of the Fe 2p regions collected for I) Fe in $MgCl_2$(aq) and II) Fe in KCl(aq). The dotted line serves as a guide, showing the Fe species is oxidized after corrosion and carbonation relative to the polished Fe surface, prior to exposure of the electrolytes.

XPS Cl 2p regions of the interface regions of the A) AFM samples and B) PM-IRRAS samples exposed to $MgCl_2$(aq) and KCl(aq), are shown in Figure S8I A-B and Figure S8II A-B, respectively. The spectra in A in panel I-II were collected after rinsing the sample with nanopure water. Here, a small amount of Cl^- is present on the interfacial area due to the incorporation of Cl^- ions into the surface.[15] The spectra of B) the interface regions, C) the submerged regions, and D) the polished regions of the Fe surface used in the PM-IRRAS experiments with $MgCl_2$(aq) (Figure S8I spectra) show the same Cl^- species with similar Cl $2p_{3/2}$ binding energies at 198.0-198.3 eV from leftover salt. Because the sample was not rinsed before collecting XPS, the substantial Cl^- signal is attributed to residual $MgCl_2$.[16] A 2nd peak at a binding energy of 199.9 eV is attributed to Fe^{2+} or Fe^{3+} chloride. Relatively more Cl^- is observed on the interface regions in 8I compared to the submerged region. Similarly, the spectra of the Cl 2p regions collected on the interface, submerged, and polished regions of Fe in KCl(aq) (Figure S8II A, B, and C spectra) contain residual Cl^-, with binding energies between 197.5-198.0 eV. The second species is only observed at the interface at 198.9-198.7 eV. Here, more Cl^- is observed in the submerged region compared to the interface region. The unexposed (polished) regions of both PM-IRRAS samples show a small amount of residual chloride from materials used to polish the surface.

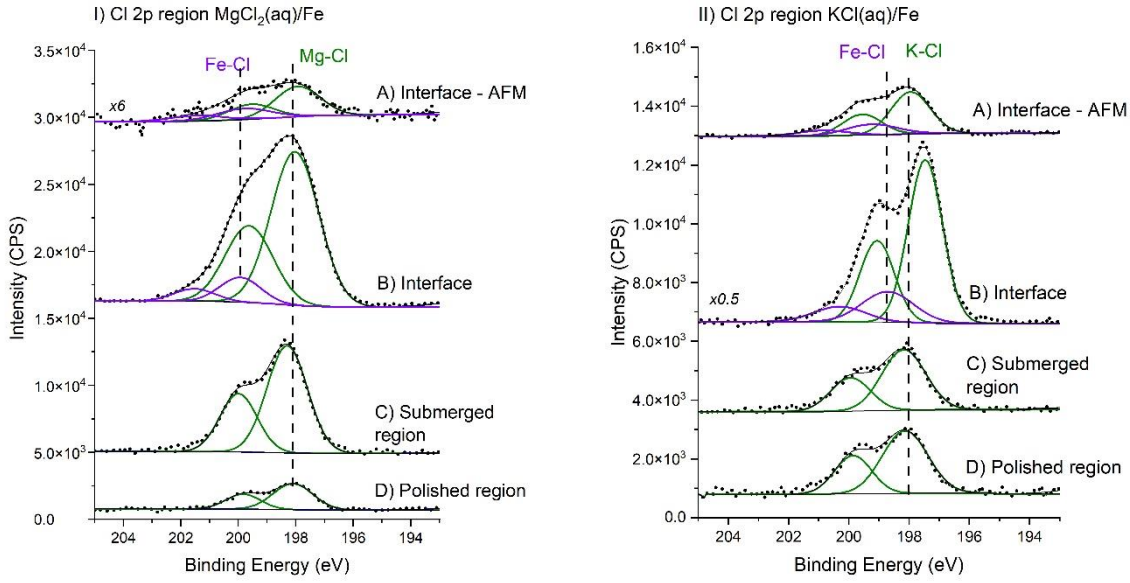

Figure S8: XPS spectra of the Cl 2p regions collected for I) Fe in $MgCl_2$(aq) and II) Fe in KCl(aq). Two species (Fe-Cl and Mg-Cl or K-Cl) are present only at the interface, from corrosion and ion deposition.

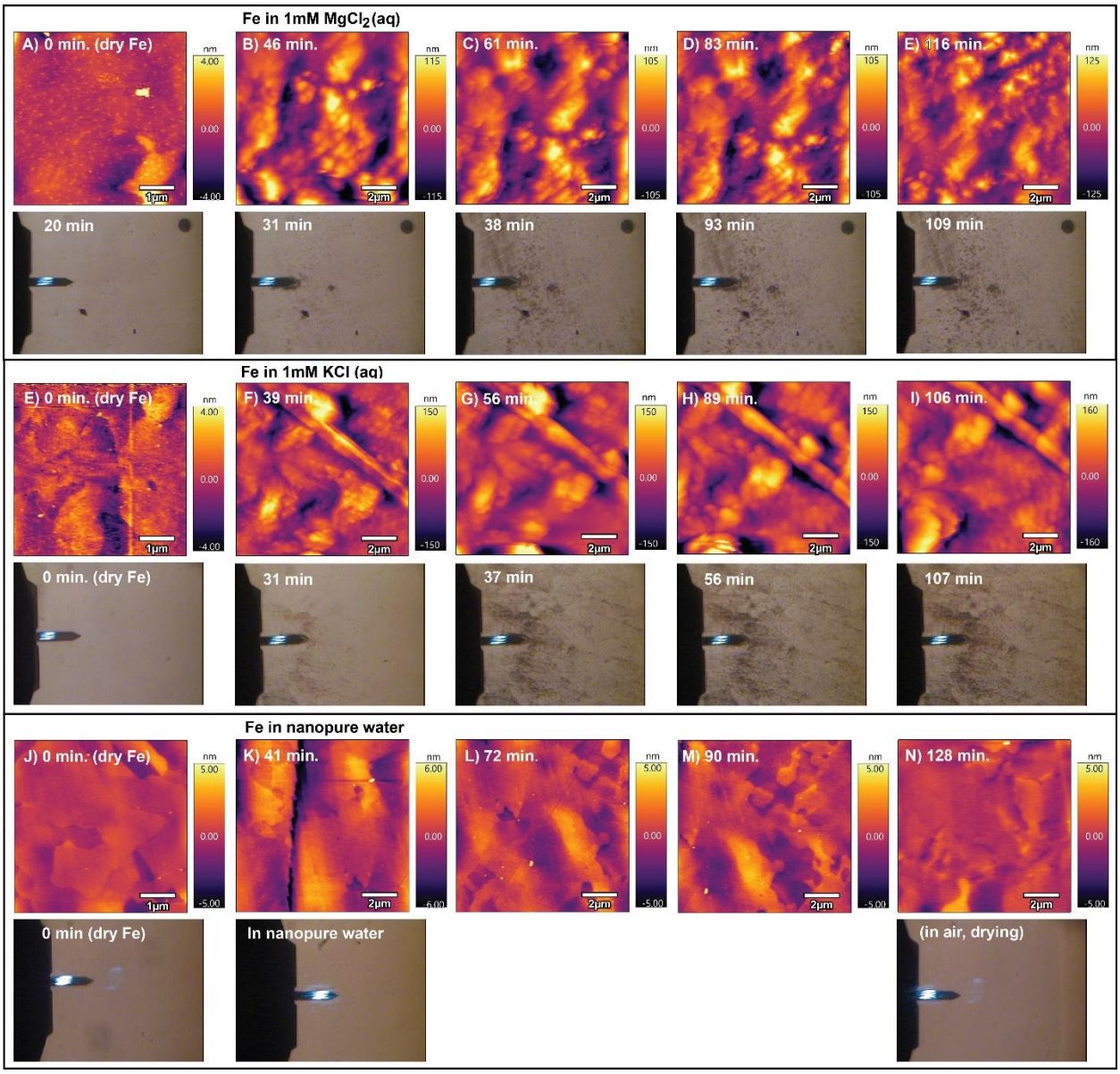

Figure S9: AFM images and photographs of the iron surface during imaging in solution. Iron was imaged in (A-E) 1 mM $MgCl_2$(aq) and (E-I) 1 mM KCl(aq). Iron was imaged in nanopure water (J-N) for comparison over the same time period. Visible corrosion occurs within 30 minutes in the photos in the chloride electrolytes and plateau in the AFM images by 40 minutes.

References

(1) Lewis, D. G.; Farmer, V. C. Infrared -Absorption of Surface Hydroxyl Groups and Lattice Vibrations in Lepidocrocite (Gamma-FeOOH) and Boehmite (Gamma-AlOOH). *Clay Minerals* **1986**, *21* (1), 93-100. DOI: 10.1180/claymin.1986.021.1.08.

(2) White, W. B. Infrared Characterization of Water and Hydroxyl Ion in the Basic Magnesium Carbonate Minerals. *The American Mineralogist* **1971**, *56*, 46-53.

(3) Frost, R. L.; Palmer, S. J. Infrared and infrared emission spectroscopy of nesquehonite Mg(OH)(HCO3)center dot 2H(2)O-implications for the formula of nesquehonite. *Spectrochimica Acta Part a-Molecular and Biomolecular Spectroscopy* **2011**, *78* (4), 1255-1260. DOI: 10.1016/j.saa.2010.12.059.

(4) Gao, W. L.; Zhou, T. T.; Wang, Q. Controlled synthesis of MgO with diverse basic sites and its CO2 capture mechanism under different adsorption conditions. *Chemical Engineering Journal* **2018**, *336*, 710-720. DOI: 10.1016/j.cej.2017.12.025.

(5) Baltrusaitis, J.; Grassian, V. H. Surface reactions of carbon dioxide at the adsorbed water-iron oxide interface. *Journal of Physical Chemistry B* **2005**, *109* (25), 12227-12230. DOI: 10.1021/jp051868k.

(6) Baltrusaitis, J.; Jensen, J. H.; Grassian, V. H. FTIR Spectroscopy combined with isotope labeling and quantum chemical calculations to investigate adsorbed bicarbonate formation following reaction of carbon dioxide with surface hydroxyl groups on Fe(2)O3 and Al2O3. *Journal of Physical Chemistry B* **2006**, *110* (24), 12005-12016. DOI: 10.1021/jp057437j.

(7) Hausner, D. B.; Bhandari, N.; Pierre-Louis, A. M.; Kubicki, J. D.; Strongin, D. R. Ferrihydrite reactivity toward carbon dioxide. *Journal of Colloid and Interface Science* **2009**, *337* (2), 492-500. DOI: 10.1016/j.jcis.2009.05.069.

(8) Khairallah, F.; Glisentia, A. XPS Study of MgO Nanopowders Obtained by Different Preparation Procedures *Surface Science Spectra* **2007**, *13*, 58-71.

(9) Kloprogge, J. T.; Wood, B. Baseline Studies of the Clay Minerals Society Source Clays by X-ray Photoelectron Spectroscopy. *Clay Science* **2018**, *22* (4), 85-94.
DOI: https://doi.org/10.11362/jcssjclayscience.22.4_85.

(10) Feliu, S.; Pardo, A.; Merino, M. C.; Coy, A. E.; Viejo, F.; Arrabal, R. Correlation between the surface chemistry and the atmospheric corrosion of AZ31, AZ80 and AZ91D magnesium alloys. *Applied Surface Science* **2009**, *255* (7), 4102-4108. DOI: 10.1016/j.apsusc.2008.10.095.

(11) Forsgren, J.; Frykstrand, S.; Grandfield, K.; Mihranyan, A.; Stromme, M. A Template-Free, Ultra-Adsorbing, High Surface Area Carbonate Nanostructure. *Plos One* **2013**, *8* (7) e68486. DOI: 10.1371/journal.pone.0068486.

(12) Mansour, A. N.; Brizzolara, R. A. Characterization of the Surface of α-FeOOH Powder by XPS *Surface Science Spectra* **1996**, *4* (357) 357–362. DOI: https://doi.org/10.1116/1.1247825.

(13) Bagus, P. S.; Nelin, C. J.; Brundle, C. R.; Crist, B. V.; Lahiri, N.; Rosso, K. M. Origin of the complex main and satellite features in Fe 2p XPS of Fe2O3. *Physical Chemistry Chemical Physics* **2022**, *24* (7), 4562-4575. DOI: 10.1039/d1cp04886d.

(14) Novotny, Z.; Mulakaluri, N.; Edes, Z.; Schmid, M.; Pentcheva, R.; Diebold, U.; Parkinson, G. S. Probing the surface phase diagram of Fe3O4(001) towards the Fe-rich limit: Evidence for progressive reduction of the surface. *Physical Review B* **2013**, *87* (19) 195410. DOI: 10.1103/PhysRevB.87.195410.

(15) Beard, B. C. Fresh Cleaved Single Crystal NaCl, XPS Spectra, Al Source *Surface Science Spectra* **1993**, *2* (91), 91-96. DOI: 10.1116/1.1247741.

(16) Siokou, A.; Kefalas, D.; Ntais, S. XPS study of hydrated MgCl₂ impregnated on flat SiO₂/Si(100) Mo and Au substrates. *Surface Science* **2003**, *532*, 472-477. DOI: 10.1016/s0039-6028(03)00207-3.